

Redox behavior and reduction mechanism of $\text{Fe}_2\text{O}_3\text{-CeZrO}_2$ as oxygen storage material

Vladimir Galvita · Kai Sundmacher

Received: 13 February 2007 / Accepted: 21 May 2007 / Published online: 28 July 2007
© Springer Science+Business Media, LLC 2007

Abstract $\text{Fe}_2\text{O}_3\text{-CeZrO}_2$ is a suitable oxygen storage material for the production of pure hydrogen by a cyclic water gas shift (CWGS) process which is based on the reduction of the material by syngas followed by the re-oxidation of the reduced material with water vapor. For identification of the reduction kinetics H_2 -temperature programmed reduction experiments were performed. Several kinetic models were tested and the activation energy of reduction was calculated by the Kissinger method, by model-based curve fitting and by the isoconversional analysis method. The reduction of $\text{Fe}_2\text{O}_3\text{-CeZrO}_2$ was found to occur in a four-step process including the reduction of Fe_2O_3 , Fe_3O_4 , and CeZrO_2 . The overall process can be interpreted as phase-boundary controlled reduction of Fe_2O_3 to Fe_3O_4 , and two-dimensional nucleation controlled reduction of Fe_3O_4 to Fe and of CeO_2 to Ce_2O_3 . At higher oxygen conversion, the reduction of Fe_3O_4 and CeO_2 are significantly influenced by volume-diffusion in the solid bulk.

Introduction

Fuel cell technology offers the possibility for highly efficient conversion of chemical energy into electricity directly

without emission of environment pollutants, thereby making fuel cells one of the most promising sources for power generation. The primary anodic fuel for fuel cells is hydrogen. Currently, steam reforming, partial oxidation and auto-thermal reforming of hydrocarbons are the major routes for hydrogen generation. By with all these methods, large amounts of CO are generated as by-product [1, 2]. Therefore, hydrogen gas being generated by these conventional processes can be utilized for low temperature Proton Exchange Membrane Fuel Cells (PEMFC) only if CO is completely eliminated from the feed stream prior to its introduction into the fuel cell. For this purpose, the product stream coming out of steam reformers containing ca. 10 vol.% CO is passed into water gas shift reactors (high temperature WGS followed by low temperature WGS) where CO reacts with water to form CO_2 and hydrogen. These reactors are the bulkiest components of the overall fuel processing system. Finally, the CO content is reduced to a few ppm in a preferential oxidation reactor. Only after this circuitous multi-unit procedure of CO-removal, the produced hydrogen gas can be fed to the fuel cell.

Recently, a novel dynamic reactor concept for the formation of highly pure hydrogen was proposed and successfully demonstrated on the laboratory scale. This concept is based on the cyclic reduction of Fe_3O_4 with methane or synthesis gas (phase 1), followed by re-oxidation of the formed iron metal with water vapor (phase 2) [3–10]:



Due to the cyclic reactor principle, in phase 1 of this process only CO_2 and water vapor are obtained as products

V. Galvita · K. Sundmacher
Otto-von-Guericke-University Magdeburg, Process Systems
Engineering, Universitätsplatz 2, 39106 Magdeburg, Germany

K. Sundmacher (✉)
Max Planck Institute for Dynamics of Complex Technical
Systems, Sandtorstraße 1, 39106 Magdeburg, Germany
e-mail: sundmacher@mpi-magdeburg.mpg.de

while in phase 2 pure hydrogen and steam are obtained which can be supplied directly to a PEMFC. The key component of the whole process is iron oxide which acts as solid oxygen storage material undergoing cyclic release and uptake of oxygen.

However, pure iron oxide was found to deactivate quickly due to sintering. The addition of CeO₂–ZrO₂ to iron oxide protects the iron metal and/or iron oxides against sintering during the redox cycle, and it increases significantly the reduction rate by H₂ and CO and also the re-oxidation rate by H₂O [10, 11].

The reduction mechanism of iron oxides including the reduction steps of Fe₂O₃ to Fe₃O₄ and Fe₃O₄ to Fe were investigated by several groups [12–16]. But the mechanism and the reduction kinetics of the mixed oxide Fe₂O₃–CeZrO₂ have not been investigated earlier. Therefore, it is the objective of the present work to present experimental data on the non-isothermal reduction of Fe₂O₃–CeZrO₂ using the H₂-TPR technique and to identify the topochemical processes occurring during the material reduction by means of model-based data analysis methods.

Kinetic analysis of TPR data

Thermo-analytical techniques are among the most important and widely used methods for the characterization of solid materials. Temperature-programmed reduction (TPR) is a convenient technique for characterizing metal oxides. TPR has been used to gain qualitative information on the reducibility of oxide species, such as metal oxides. Kinetic interpretation of TPR data is normally based on the following general kinetic equation [17–19]:

$$\frac{d\alpha}{dt} = k(T) \cdot f_1(\alpha) \cdot f_2(C_{H_2}, C_{H_2O}) \tag{3}$$

where α is the degree of conversion of mobile oxygen in the solid reactant, $k(T)$ is the temperature-dependent rate coefficient, $f_1(\alpha)$ represents the dependence of reduction kinetics on solid conversion, and $f_2(C_{H_2}, C_{H_2O})$ expresses the dependence on the gas-phase concentrations of hydrogen and water. The rate coefficient $k(T)$ is typically expressed by an Arrhenius-type equation:

$$k(T) = A \cdot \exp\left(-\frac{E}{RT}\right) \tag{4}$$

For a heating program at constant heating rate β the temperature change is given by:

$$dT = \beta dt \tag{5}$$

By combining Eqs. 3–5, we get

$$\frac{d\alpha}{dT} = \frac{A}{\beta} \cdot \exp\left(\frac{-E}{RT}\right) \cdot f_1(\alpha) \cdot f_2(C_{H_2}, C_{H_2O}) \tag{6}$$

The TPR response curve is obtained by integrating Eq. 6:

$$\int_0^\alpha \frac{d\alpha}{f_1(\alpha)} = g(\alpha) = \frac{A}{\beta} \cdot \int_{T_0}^T \exp\left(\frac{-E}{RT}\right) dT \cdot f_2(C_{H_2}, C_{H_2O}) \tag{7}$$

The most frequently applied kinetic models can be categorized into three groups which describe diffusion-controlled processes, boundary-controlled processes, and processes involving random nucleation and subsequent growth of nuclei, see e.g. [19]. Algebraic expressions for $f(\alpha)$ and $g(\alpha)$ for each of these models are listed in Table 1 [19, 20]. For diffusion-controlled processes, the overall rate is determined by the movement of one or more reactant species to or a product from a reaction interface inside the material. Phase boundary-controlled models are geometrically defined as shrinking/unreacted cores or contracting spheres where the reaction is the rate-determining step which proceeds topochemically. Regarding the reduction of metal oxides, nucleation-controlled processes involve uniform internal reduction and occur by the initial random removal of lattice oxygen atoms until a critical concentration of vacancies is reached. The vacancies are then annihilated by lattice rearrangement to produce metal nuclei. The nuclei then grow and, as they expand, the reduction process accelerates due to the increasing metal–metal oxide interface which is further increased by the formation of new nuclei. Eventually, merging of product nuclei causes a decrease in sample-product interfacial area and the reduction decelerates. Autocatalytic mechanisms, where the product metal enhances the dissociation of hydrogen molecules thereby increasing the rate of reduction

Table 1 Possible controlling mechanisms for solid-state reactions

Mechanisms	$f(\alpha)$	$g(\alpha)$
1 Random nucleation	$(1-\alpha)$	$-\ln(1-\alpha)$
2 Contracting area	$(1-\alpha)^{1/2}$	$2(1-(1-\alpha)^{1/2})$
3 Contracting volume	$(1-\alpha)^{1/3}$	$3(1-(1-\alpha)^{1/3})$
4 1D Avrami-Erofeyev	$2(1-\alpha)(\ln(1-\alpha))^{1/2}$	$(-\ln(1-\alpha))^{1/2}$
5 2D Avrami-Erofeyev	$3(1-\alpha) \ln(1-\alpha)^{2/3}$	$(-\ln(1-\alpha))^{1/3}$
6 3D Avrami-Erofeyev	$4(1-\alpha)(\ln(1-\alpha))^{2/3}$	$(-\ln(1-\alpha))^{1/4}$
7 One-dimensional diffusion	$1/2\alpha$	α^2
8 Three-dimensional diffusion	$3(1-\alpha)^{2/3}/(2(1-(1-\alpha)^{1/3}))$	$(1-(1-\alpha)^{1/3})^2$

of remaining metal oxide, have also to be accounted for when studying solid–gas reductions.

There are several methods for the identification of activation energies from TPR data. Kissinger [21] proposed a method for evaluating the activation energy E from the shift of the temperature at which the reduction rate has a maximum, T_{\max} , by variation of the heating rate β . The quantity $\ln(\beta/T_{\max}^2)$ is plotted versus $1/T_{\max}$ for different heating rates in order to obtain an Arrhenius-type diagram where $(-E/R)$ is identified as the slope of the curve.

Alternatively, Friedman's isoconversional method allows the determination of model-independent estimates of the activation energy [22, 23]. Also here, a series of experiments has to be conducted at different heating rates. Then, one can apply the isoconversional principle, according to which the reaction rate at constant extent of conversion is only a function of the temperature:

$$\left[\frac{d \ln(dx/dt)}{dT^{-1}} \right]_{\alpha} = -E/R. \quad (8)$$

Experimental

Material preparation

In the present study Fe_2O_3 , (30 wt.%- Fe_2O_3)- $\text{Ce}_{0.5}\text{Zr}_{0.5}\text{O}_2$ and $\text{Ce}_{0.5}\text{Zr}_{0.5}\text{O}_2$ were compared as possible oxygen storage materials for the considered redox process. The preparation of the Fe_2O_3 - $\text{Ce}_{0.5}\text{Zr}_{0.5}\text{O}_2$ and $\text{Ce}_{0.5}\text{Zr}_{0.5}\text{O}_2$ samples was based on urea hydrolysis [24, 25] using $\text{Fe}(\text{NO}_3)_3 \cdot 9\text{H}_2\text{O}$ (99.0%, Fluka), $\text{Ce}(\text{NO}_3)_3 \cdot 6\text{H}_2\text{O}$ (99.0%, Fluka) and $\text{ZrO}(\text{NO}_3)_2 \cdot 6\text{H}_2\text{O}$ (99.0%, Fluka) as starting materials. Details of the material preparation route are described in our previous paper [11].

Temperature programmed reduction

Temperature programmed reduction measurements were carried out to investigate the redox properties over the resulting materials. A sample of 20 mg was placed in an U-shaped quartz tube and was pretreated in Argon atmosphere (flow rate 30 mL/min) at 140 °C for 60 min before the TPR experiment was started. After pretreatment the samples were heated from 140 °C to 850 °C at heating rates $\beta = 4, 10$ or 15 °C/min. The reducing feed gas contained 10 vol.% H_2 in Ar at a total flow rate of 30 mL/min. The hydrogen consumption was monitored using a thermal conductivity detector.

The selection of experimental conditions was in agreement with the criterion being developed by Maler and Caballero, $P = \beta \times S_0 / (F \times C_0) \ll 20 \text{ K}$ (β : heating rate; S_0 :

initial molar amount of reducible substance; F : volumetric flow rate of reducing agent; C_0 : molar concentration of reducing agent). The instantaneous maximum conversion of hydrogen was less than 15% in our system.

Material characterization techniques

Phase characterization was carried out by XRD using $\text{Cu-K}\alpha$ radiation. The data were collected in the 2θ range from 10° to 80° in 0.01° steps. The Brunauer–Emmett–Teller (BET) surface area was determined by N_2 adsorption at 77 K (five point BET method using the NOVA 2000e device). Prior to the analysis, the samples were out-gassed to eliminate volatile adsorbents on the surface at 250 °C for 4 h.

Estimation of kinetic parameters

Kinetic parameters E and A in Eq. 7 were estimated using nonlinear regression method based on the Levenberg–Marquardt algorithm. The integral equation (Eq. 7) was numerically solved. All the computations were performed in the ORIGIN 7 environment.

Results

Characterization of Fe_2O_3 - $\text{Ce}_{0.5}\text{Zr}_{0.5}\text{O}_2$ by powder XRD and SEM

X-ray diffractograms of Fe_2O_3 - $\text{Ce}_{0.5}\text{Zr}_{0.5}\text{O}_2$ and $\text{Ce}_{0.5}\text{Zr}_{0.5}\text{O}_2$ are shown in Fig. 1. Freshly prepared and

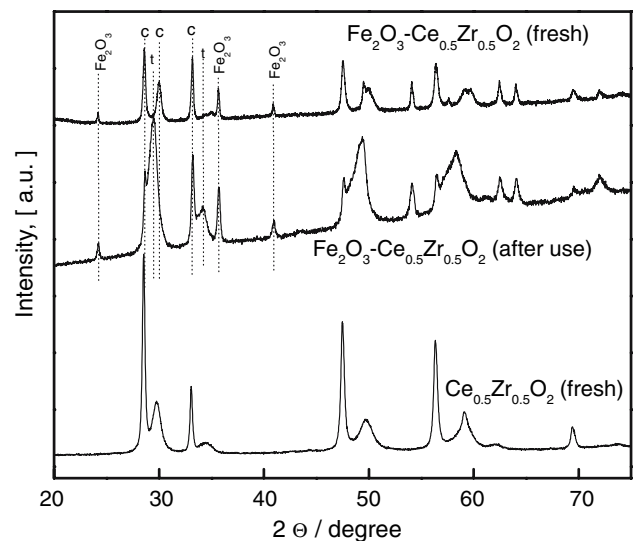


Fig. 1 XRD patterns of freshly prepared and reduced/re-oxidized samples: (a) $\text{Ce}_{0.5}\text{Zr}_{0.5}\text{O}_2$, (b) 30 wt.% Fe_2O_3 - $\text{Ce}_{0.5}\text{Zr}_{0.5}\text{O}_2$, (c) 30 wt.% Fe_2O_3 - $\text{Ce}_{0.5}\text{Zr}_{0.5}\text{O}_2$ after re-oxidation; c: cubic phase of $\text{Ce}_{0.5}\text{Zr}_{0.5}\text{O}_2$, t: tetragonal phase of $\text{Ce}_{0.5}\text{Zr}_{0.5}\text{O}_2$

used (after the redox cycling) $\text{Fe}_2\text{O}_3\text{-Ce}_{0.5}\text{Zr}_{0.5}\text{O}_2$ samples yielded all characteristic reflections which correspond to $\alpha\text{-Fe}_2\text{O}_3$, a cubic structure of a ceria-rich solid solution with zirconia and a tetragonal structure of a zirconia-rich solid solution with ceria. Small amounts of zirconium oxide were detected only in fresh $\text{Fe}_2\text{O}_3\text{-Ce}_{0.5}\text{Zr}_{0.5}\text{O}_2$ samples. XRD analysis revealed that no binary compounds were formed between Fe-oxides and Ce-oxides. FeCeO_3 compounds with the cerium ions being in the Ce^{3+} state were identified neither in fresh $\text{Fe}_2\text{O}_3\text{-CeZrO}_2$ samples nor in re-oxidized samples after several redox cycles. The particle diameter which was calculated by the XRD line broadening method increased from 50 nm (fresh material) to 150 nm (after redox cycles). The BET surface area of $\text{Fe}_2\text{O}_3\text{-Ce}_{0.5}\text{Zr}_{0.5}\text{O}_2$ was found to decrease during reduction/oxidation cycles from $10\text{ m}^2/\text{g}$ to $7\text{ m}^2/\text{g}$. Figure 2 presents a scanning electron microscopy (SEM) image of the fresh $\text{Fe}_2\text{O}_3\text{-Ce}_{0.5}\text{Zr}_{0.5}\text{O}_2$.

Reduction properties of Fe_2O_3 and $\text{Fe}_2\text{O}_3\text{-Ce}_{0.5}\text{Zr}_{0.5}\text{O}_2$ samples

The H_2 -TPR behavior of a freshly prepared $\text{Fe}_2\text{O}_3\text{-Ce}_{0.5}\text{Zr}_{0.5}\text{O}_2$ sample during several subsequent re-oxidation and reduction cycles is plotted in Fig. 3. Three peaks at about 400, 550 and 750 °C are observed. Upon further recycling through repetitive reduction/oxidation steps, the TPR profile still changes to reach its final form after the 4th cycle showing two sharp peaks centered at 396–400 °C and 564–566 °C and a third very flat peak at 725–775 °C. The reduction is complete at temperatures above 850 °C.

The attribution of the reduction peaks to individual mechanistic steps is not easy for the mixed oxide $\text{Fe}_2\text{O}_3\text{-Ce}_{0.5}\text{Zr}_{0.5}\text{O}_2$, because of partial peak overlapping caused

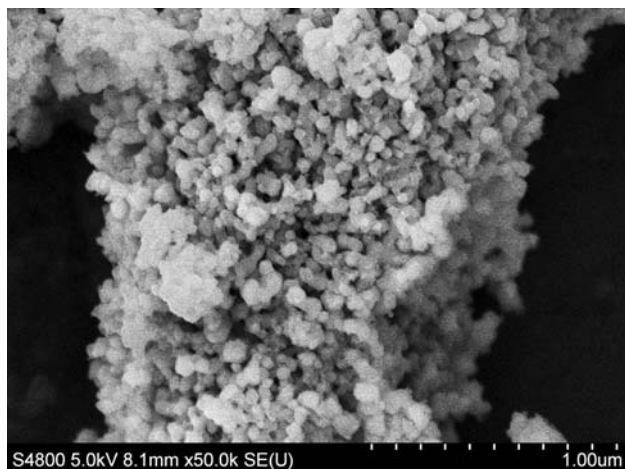


Fig. 2 SEM micrograph of reduced/re-oxidized $\text{Fe}_2\text{O}_3\text{-Ce}_{0.5}\text{Zr}_{0.5}\text{O}_2$ sample

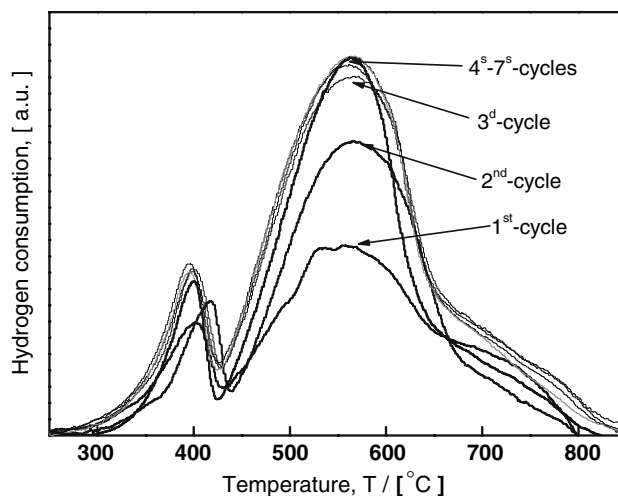


Fig. 3 Experimental H_2 -TPR data for $\text{Fe}_2\text{O}_3\text{-Ce}_{0.5}\text{Zr}_{0.5}\text{O}_2$ at different numbers of subsequent reduction and re-oxidation cycles

by the simultaneous reduction of the oxides Fe_2O_3 , Fe_3O_4 and CeZrO_2 . The reduction of iron oxide by hydrogen is known to be a two-stage process [17–20] where Fe_2O_3 first is reduced to Fe_3O_4 which is further reduced to metallic iron. The reduction of CeZrO_2 by hydrogen is also a two-stage process including surface and bulk reduction steps [26].

To be able to deconvolute the TPR spectrum of the mixed oxide $\text{Fe}_2\text{O}_3\text{-Ce}_{0.5}\text{Zr}_{0.5}\text{O}_2$ into individual contributions, additional experiments with Fe_2O_3 and $\text{Ce}_{0.5}\text{Zr}_{0.5}\text{O}_2$ were performed. Figure 4 shows the corresponding TPR profiles along with the profile of the mixed oxide $\text{Fe}_2\text{O}_3\text{-Ce}_{0.5}\text{Zr}_{0.5}\text{O}_2$. The peaks in the profiles are

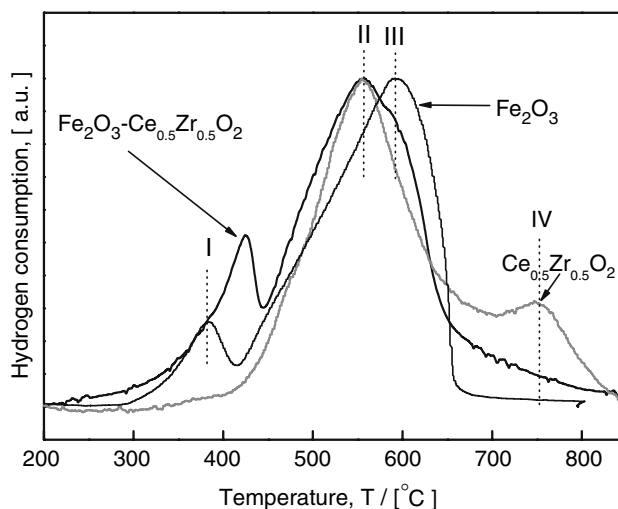
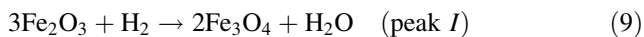
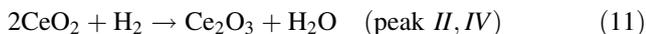


Fig. 4 Comparison of experimental H_2 -TPR profiles for Fe_2O_3 , $\text{Ce}_{0.5}\text{Zr}_{0.5}\text{O}_2$, and $\text{Fe}_2\text{O}_3\text{-Ce}_{0.5}\text{Zr}_{0.5}\text{O}_2$ samples; heating rate: $\beta = 10\text{ }^\circ\text{C}/\text{min}$

designated as *I*, *II*, *III* and *IV*. The peaks *I* and *III* can be attributed to the reduction of iron oxides



while the peaks *II* and *IV* are related to the reduction of $\text{Ce}_{0.5}\text{Zr}_{0.5}\text{O}_2$:



In accordance with Eqs. 9 and 10, for Fe_2O_3 two TPR peaks were observed. The low-temperature peak *I* at 379 °C can be assigned to the reduction of Fe_2O_3 to Fe_3O_4 while the high-temperature peak *III* at 592 °C is due to the reduction of Fe_3O_4 to Fe. For the mixed oxide $\text{Ce}_{0.5}\text{Zr}_{0.5}\text{O}_2$ two peaks were observed as well. The large low-temperature peak *II* at 550 °C is supposed to be attributable mainly to the reduction of oxygen species of the cubic ceria-rich phase, while peak *IV* at 752 °C is supposed to be related to reduction processes occurring in the zirconia-rich tetragonal phase. Furthermore, different activation energies for the reduction of surface and bulk oxygen may be responsible for peaks *II* and *IV*.

Overall, one can see that the TPR profile of the mixed oxide $\text{Fe}_2\text{O}_3\text{-Ce}_{0.5}\text{Zr}_{0.5}\text{O}_2$, which shows two pronounced peaks and one flat peak, is caused by the superposition of the TPR spectra of Fe_2O_3 and $\text{Ce}_{0.5}\text{Zr}_{0.5}\text{O}_2$. The small low-temperature peak is caused by Fe_2O_3 to Fe_3O_4 reduction, the main peak is created by the overlapping peaks *II* (Fe_3O_4 to Fe) and *III* (CeO_2 to Ce_2O_3 at surface), and the final flat peak mainly comes CeO_2 to Ce_2O_3 reduction.

Kinetic analysis of TPR experiments

As first step for TPR data analysis, the peak positions and profiles can be roughly described by Gaussian functions. Thus, the reduction profiles presented in Fig. 5 for the $\text{Fe}_2\text{O}_3\text{-Ce}_{0.5}\text{Zr}_{0.5}\text{O}_2$ sample were deconvoluted into four Gaussian-type profiles taking into account the stoichiometric H_2 -consumptions as defined by Eqs. 9–11 and the material amount and composition. The comparison of the experimental and fitted reduction profiles being presented in Fig. 5 clearly shows that the deconvolution into 4 peaks gives a reasonable fit of the experimental TPR profile. However, the Gaussian-type deconvolution does not give any insight into details of the reduction mechanism. In order to identify the mechanisms of all involved reduction steps, the following procedure was applied: First activation energies were determined from the deconvoluted Gaussian peaks using the Kissinger method [21]; second, these values were taken as starting parameters for a least squares

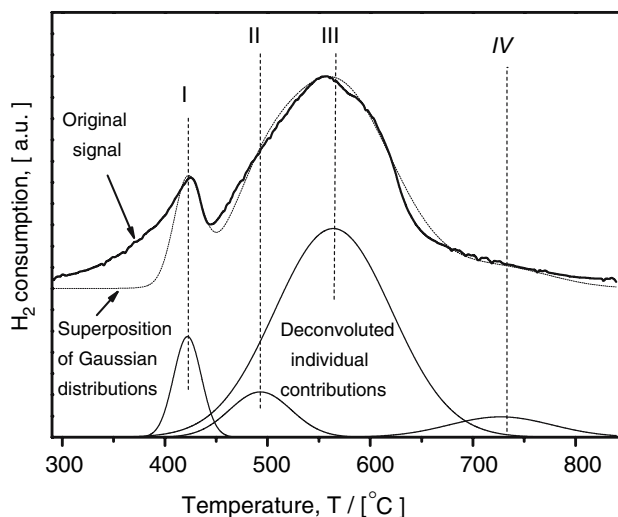


Fig. 5 Comparison of H_2 -TPR profiles of $\text{Fe}_2\text{O}_3\text{-Ce}_{0.5}\text{Zr}_{0.5}\text{O}_2$ after four reduction/re-oxidation cycles: Experimental data, deconvoluted individual contributions and superposition of Gaussian distributions; heating rate: $\beta = 10$ °C/min

fitting procedure using selected mechanistic models, as collected in Table 1, for the representation of each individual peak.

Temperature-programmed reduction profiles obtained at different heating rates (4, 10 and 15 °C/min) are shown in Fig. 6. An increase in the heating rate from 4 °C/min to 15 °C/min leads to a shift of the peak maximum temperatures by 49 and 97 °C for the first and the second step of iron reduction, respectively. Figure 7 shows the Arrhenius plots based on Kissinger's method, i.e. $\ln(\beta/T_{\text{max}}^2)$ versus $1/T_{\text{max}}$, using the TPR data being obtained at the three heating rates. The estimated activation energies for the four reduction steps of the $\text{Fe}_2\text{O}_3\text{-Ce}_{0.5}\text{Zr}_{0.5}\text{O}_2$ sample are $E_I = 104$ kJ/mol, $E_{II} = 80$ kJ/mol, $E_{III} = 71$ kJ/mol and $E_{IV} = 64$ kJ/mol.

In the second step of our analysis, various mechanistic reduction models (from Table 1) were now tested by least squares fitting of each of the four peaks appearing in the TPR spectrum of $\text{Fe}_2\text{O}_3\text{-Ce}_{0.5}\text{Zr}_{0.5}\text{O}_2$. The model quality was evaluated by the residue of the objective function at the optimum. Thereby, most probable reduction models were selected from Table 1 for each of the four involved reduction steps along with related values for the activation energies.

Peak *I* was best fitted by the phase boundary controlled model for the reaction of Fe_2O_3 to Fe_3O_4 . The further reduction of Fe_3O_4 to Fe (peak *III*) was fitted with the two-dimensional nucleation model of Avrami-Erofeyev. The reduction of $\text{Ce}_{0.5}\text{Zr}_{0.5}\text{O}_2$ in peak *II* was controlled by the same mechanism (2D nucleation) while for peak *IV* the diffusion-control model yields the best fitting result.

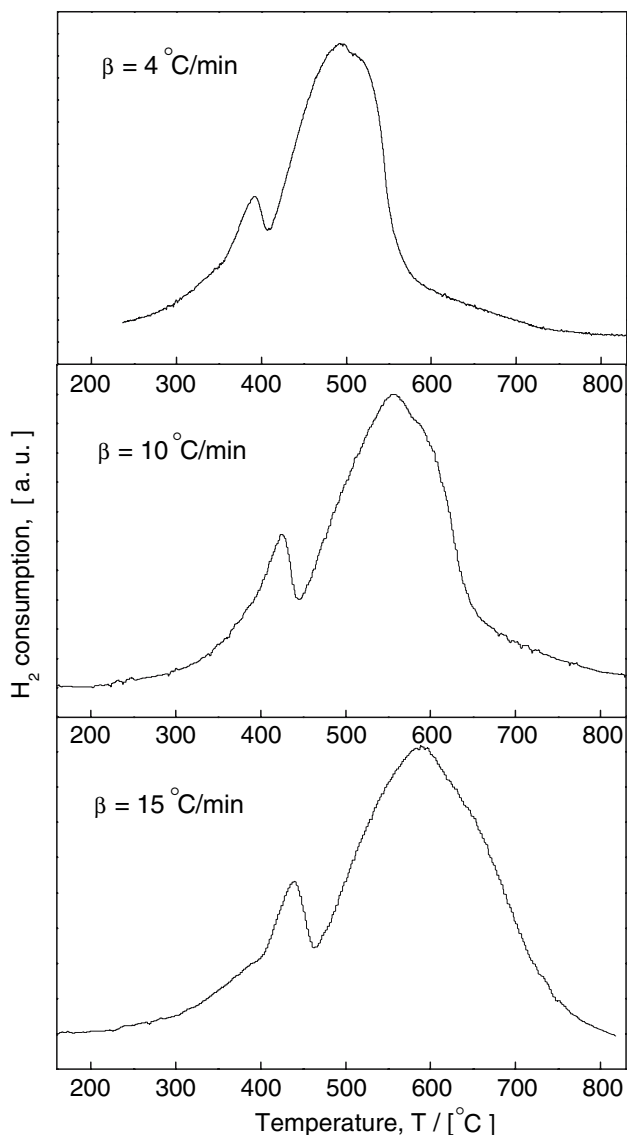


Fig. 6 Experimental H₂-TPR profiles of Fe₂O₃-Ce_{0.5}Zr_{0.5}O₂ at three different heating rates

Table 2 summarizes the findings of this work as well as of previous studies of other authors and gives the related values of activation energies. In the literature, the reduction of Fe₂O₃ to Fe₃O₄ was found to follow a random nucleation mechanism, while in this work a contracting area model, i.e. a sharp interface-controlled reaction as governing mechanistic step, is favored. Concerning the reduction of Fe₃O₄ to Fe, we found the 2D nucleation model of Avrami-Erofeyev to be the most appropriate description being in agreement with [13, 14], whereas in [12] a 3D Avrami-Erofeyev mechanism was postulated. These mechanistic discrepancies may arise from the use of different particle sizes in the investigations of different authors. With increasing particle size, the literature indicates that the rate limiting step shifts from nucleation

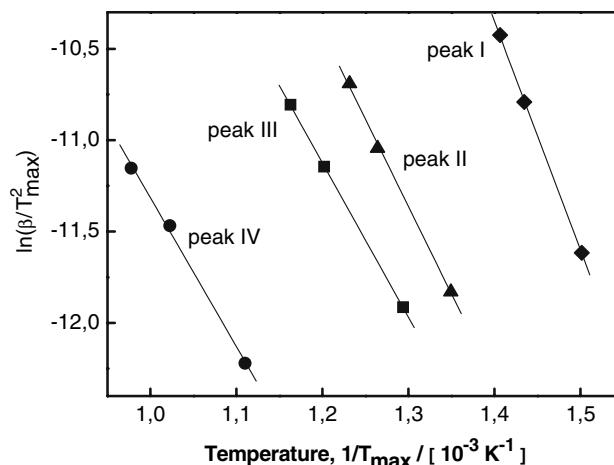


Fig. 7 Arrhenius plots for temperature-programmed reduction (H₂-TPR) of Fe₂O₃-Ce_{0.5}Zr_{0.5}O₂ sample, based on the TPR peak data in Fig. 6 with after Gaussian deconvolution

phenomena to phase boundary-controlled chemical reactions at the Fe₃O₄/Fe metal interface and/or diffusion processes through the metallic Fe product layer [12].

Regarding the reduction of CeO₂, a diffusion controlled mechanism is favored in the literature [27–30], while in the present study a 2D Avrami-Erofeyev nucleation model fits the TPR peak best and the diffusion model was identified from peak IV only. For the interpretation of this finding, one has to keep in mind that in [28–30] pure CeO₂ material was used, whereas in the present study we prepared mixed solid solutions of CeO₂ in ZrO₂ as part of the mixed oxide Fe₂O₃-Ce_{0.5}Zr_{0.5}O₂. Oxygen ions will have a higher mobility in zirconia-doped ceria and in ceria-doped zirconia. Consequently, the diffusion rate in these solutions will be higher, too.

Figure 8a shows experimental and calculated TPR patterns at the heating rate $\beta = 10$ K/min. Obviously, the model curve fits the experimental TPR profile quite well. The deconvolution of the TPR spectrum of Fe₂O₃-Ce_{0.5}Zr_{0.5}O₂ into individual mechanistic contributions is depicted in Fig. 8b. The relative amounts of hydrogen consumption for peak I (Fe₂O₃ to Fe₃O₄), peak III (Fe₃O₄ to Fe) and the sum of peaks II and IV (CeO₂ to Ce₂O₃) are 1:7:2.5. From the stoichiometric composition of the prepared sample the expected relative amounts are 1:8:1.9. Thus, first one can conclude that not all of the stoichiometrically stored oxygen is accessible for reduction by hydrogen. Second, in the temperature range of peak III the reduction of Fe₃O₄ to metallic Fe is incomplete. The remaining Fe₃O₄ is fully reduced at temperatures above 650 °C such that peak IV is a lumped signal for the reduction of CeO₂ to Ce₂O₃ and of Fe₃O₄ to Fe.

Another technique to extract activation energies from TPR spectra is the model-free isoconversional method.

Table 2 Identified reduction mechanisms, activation energies and pre-exponential factor for individual reduction steps

Reduction step	Reduction mechanism	A, s^{-1}	$E, kJ/mol$	Source
$Fe_2O_3 \rightarrow Fe_3O_4$ (peak I)	Random nucleation		74–117	[13]
			96	[14]
	Contracting area (= sharp interface controlled reaction)	$1.2 \pm 0.2 \cdot 10^6$	$104 \pm 15^*$	This work
$Fe_3O_4 \rightarrow Fe$ (peak III)	2D Avrami-Erofeyev		70.4	[13]
			59–69	[14]
		330 ± 60	$78 \pm 12^*$	This work
$CeO_2 \rightarrow Ce_2O_3$ (peaks II, IV)	3D Avrami-Erofeyev		111	[12]
	Diffusion control		95	[28]
	Diffusion control		127	[29]
	2DAvrami-Erofeyev (peak II)	$1.45 \pm 0.2 \cdot 10^3$	$83 \pm 15^*$	This work
	Diffusion control (peak IV)	30 ± 7	$66 \pm 13^*$	

* Obtained from experiments with $Fe_2O_3-Ce_{0.5}Zr_{0.5}O_2$

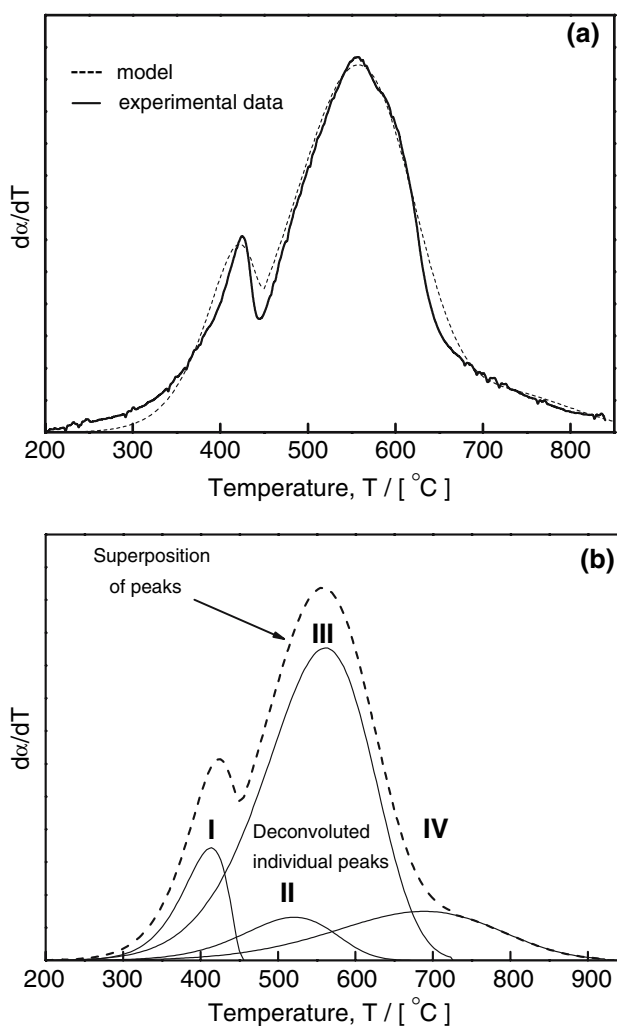


Fig. 8 (a) Calculated H_2 -TPR peaks based on reduction mechanisms being identified in this work as given in Table 2; heating rate: $\beta = 10 \text{ }^\circ\text{C}/\text{min}$. (b) Comparison of experimental and simulated H_2 -TPR profiles at heating rate $\beta = 10 \text{ }^\circ\text{C}/\text{min}$

This method uses rate data at constant conversion which allows to eliminate the dependence of the reaction rate on the conversion. Kinetic parameters are obtained by plotting $\ln(d\alpha/dt)$ against $1/T$ in the conversion interval from $\alpha = 0.2$ – 0.9 . Thus, for each α -value one gets one value for the (effective) activation energy (see Fig. 9). For the reduction of $Fe_2O_3-Ce_{0.5}Zr_{0.5}O_2$ it can be seen that the effective activation energy decreases from 87 kJ/mol at $\alpha = 0.2$ –65 kJ/mol at $\alpha = 0.9$ over the course of reduction as illustrated in Fig. 9.

The results of the Kissinger method, the model-based peak deconvolution analysis and the isoconversional method analysis agree qualitatively well. But the whole analysis clearly reveals that the overall reduction of the considered mixed oxide is a complex multi-step process where each step can be influenced by nucleation, interfacial

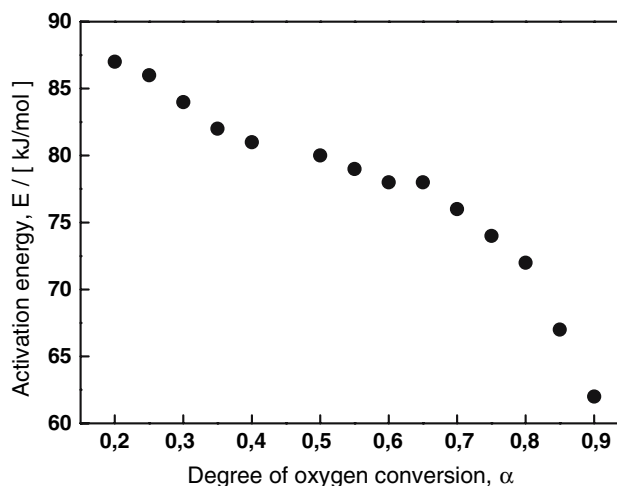


Fig. 9 Activation energy versus degree of oxygen conversion for $Fe_2O_3-Ce_{0.5}Zr_{0.5}O_2$ reduction

reaction and also by solid phase diffusional transport. These influences can overlap such that the deconvolution into simple mechanistic steps does not always yield a unique solution. In other words, for a more detailed identification of mechanisms being responsible for the TPR spectrum of $\text{Fe}_2\text{O}_3\text{-Ce}_{0.5}\text{Zr}_{0.5}\text{O}_2$ there is a need for a sophisticated reduction model including all redox reactions and physical transport phenomena.

Conclusions

The redox behavior and reduction mechanism of the mixed oxide $\text{Fe}_2\text{O}_3\text{-Ce}_{0.5}\text{Zr}_{0.5}\text{O}_2$ were studied using the H_2 -TPR technique. Classical kinetic models were applied and activation energies of reduction were determined using three different analysis methods (Kissinger method, model-based peak deconvolution, isoconversional method). The reduction of $\text{Fe}_2\text{O}_3\text{-Ce}_{0.5}\text{Zr}_{0.5}\text{O}_2$ was found to be a complex process including the reductions of Fe_2O_3 , Fe_3O_4 , and $\text{Ce}_{0.5}\text{Zr}_{0.5}\text{O}_2$ being dominated by different physico-chemical mechanisms. The reduction of Fe_2O_3 to Fe_3O_4 can be interpreted as phase-boundary controlled reaction being followed by the nucleation-controlled reduction of Fe_3O_4 to Fe, and the simultaneous reduction of CeO_2 to Ce_2O_3 being also controlled by 2D nucleation. At higher oxygen conversion, the reduction steps of Fe_3O_4 to Fe and of CeO_2 to Ce_2O_3 are controlled by solid phase diffusion. The proposed mechanism was used for TPR simulation. The simulated TPR agrees well with the experimental one.

Acknowledgements Funding for this research work by the German federal state of Saxony-Anhalt within the joint project “Dezentrales Brennstoffzellen-basiertes Energieerzeugungssystem für den stationären Betrieb in der Leistungsklasse 20 kW” is gratefully acknowledged. The authors are also very thankful to Dr. Heike Lorenz, Max-Planck-Institute in Magdeburg, for her support in performing the XRD measurements, and to Dr. Veit, Institute for Experimental Physics of Magdeburg University, for preparing SEM images of our materials.

References

1. Krumpelt M, Krause TR, Carter JD, Kopasz JP, Ahmed S (2002) *Catal Today* 77:3
2. Armor JN (1999) *Appl Catal A Gen* 176:159
3. Fukase S, Suzuka T (1993) *Appl Catal A Gen* 100:1
4. Hacker V, Faleschini G, Fuchs H, Fankhauser R, Simader G, Ghaemi M, Spreity B, Friedrich K (1998) *J Power Sources* 71:226
5. Hacker V, Fankhauser R, Faleschini G, Fuchs H, Friedrich K, Muhr M, Kordesch K (2000) *J Power Sources* 86:531
6. Hacker V (2003) *J Power Sources* 118:311
7. Takenaka S, Son VTD, Hanaizumi N, Nomura K, Otsuka K (2004) Proceedings of 13th International Conference on Catalysis. 11–16 July 2004, Paris, France
8. Rossini S, Cornaro U, Mizia F, Malandrino A, Piccoli V, Sanfilippo D, Miracca I (2003) In: Eming G, Ernst S, Harth K, Rupp M (eds) Proceedings of the DGMK-Conference Innovation in the manufacture and use of hydrogen. 15–17 October, Dresden, Germany, pp 41–47
9. Otsuka K, Yamada C, Kaburagi T, Takenaka S (2003) *Int J Hydrogen Energy* 28:335
10. Galvita V, Sundmacher K (2005) *Appl Catalysis A Gen* 289:121
11. Galvita V, Sundmacher K (2005) Proceedings of 4th International Conference on environmental catalysis. 5–8 June, Heidelberg, Germany, p 270
12. Wimmers OJ, Arnoldy P, Moulijn JA (1986) *J Phys Chem* 90:1331
13. Tiernan MJ, Barners PA, Parkers GMB (2001) *J Phys Chem* 105:220
14. Lin HY, Chen YW, Li C (2003) *Thermochim Acta* 400:61
15. Tiernan MJ, Barner PA, Parkes GMB (2001) *J Phys Chem B* 105:220
16. Piotrowski K, Maondal K, Lorethova H, Stonawski L, Szymanski T, Wiltowski T (2005) *Int J Hydrogen Energy* 30:1543
17. Wimmers OJ, Arnoldy P, Moulijn AJ (1986) *J Phys Chem* 90:1331
18. Kanervo JM, Krause AOI (2001) *J Phys Chem* 105:9778
19. Rown WE, Dollimore D, Galwey AK (1980) In: Bamford CH (ed) Chemical kinetics, reaction in the solid state, vol 22. Elsevier, Oxford New York, p 307
20. Kanervo JM (2003) Kinetic analysis of temperature-programmed reaction. Industrial Chemistry publication Series, No 16, Espoo, p 70
21. Kissinger HE (1957) *Analyt Chem* 29:1702
22. Friedman HL (1965) *Polym Sci Part C* 6:183
23. Vyazovkin S, Wight CA (1997) *Annu Rev Chem* 48:125
24. Pengpanich S, Meeyoo V, Rirksoomboon T, Bunyakiat K (2002) *Appl Catal A Gen* 234:221
25. Subrt J, Bohacek J, Stengl V, Grygar T, Bezdicka P (1999) *Mat Res Bull* 34:905
26. Fornasiero P, Balducci G, Di Monte R, Kaspar J, Sergio V, Gubitosa G, Ferrero A, Graziani M (1996) *J Catal* 164:173
27. Fan J, Wu X, Ran R, Weng D (2005) *Appl Surf Sci* 245:162
28. Al-Madfaa HA, Khader MM (2004) *Mater Chem Phys* 86:180
29. Munteanu G, Ilieva L, Nedyalkova R, Andreeva D (2004) *Appl Catal A Gen* 277:31
30. Giordano F, Trovarelli A, de Leitenburg C, Giona M (2000) *J Catal* 193:273